Mechanical breakdown of bent silicon nanowires imaged by coherent x-ray diffraction

Mechanical breakdown of bent silicon nanowires imaged by coherent x-ray diffraction

Xiaowen Shi[1,4,5]**, Jesse N Clark**[1]**, Gang Xiong**[1]**,
Xiaojing Huang**[1,2,6]**, Ross Harder**[2] **and Ian K Robinson**[1,3,7]

[1] London Centre for Nanotechnology and Department of Physics and
Astronomy, University College London, Gower Street, London WC1E 6BT, UK
[2] Advanced Photon Source, Argonne National Laboratory, 9700 S Cass Avenue
Argonne IL 60439, USA
[3] Research Complex at Harwell, Didcot, Oxfordshire OX11 0DE, UK
E-mail: i.robinson@ucl.ac.uk

Abstract. We have developed a method of coherent x-ray diffractive imaging to surmount its inability to image the structure of strongly strained crystals. We used calculated models from finite–element analysis to guide an iterative algorithm to fit experimental data from a series of increasingly bent wires cut into silicon-on-insulator films. Just before mechanical fracture, the wires were found to contain new phase structures, which are identified as dislocations associated with crossing the elastic limit.

[4] Present Address: Advanced Light Source, Lawrence Berkeley National Laboratory, Berkeley, California 94720, USA

[5] Present Address: Department of Physics, University of Oregon, Eugene, Oregon 97403, USA.

[6] Present Address: National Synchrotron Light Source II, Brookhaven National Laboratory, Upton, NY 11973 USA.

[7] Author to whom any correspondence should be addressed.

IOP Institute of Physics **◆** DEUTSCHE PHYSIKALISCHE GESELLSCHAFT

Contents

1. Elastic limit of single-crystalline silicon and associated dislocations

Materials undergo elastic deformation whereby the applied external stress and the resulting strain follow a linear relationship, as can be nicely illustrated in stress–strain diagrams. However, when the applied external stresses exceed the elastic limit of the material, the linear stress–strain relation does not hold anymore. The elastic limit, where the linear region ends, for single-crystalline silicon is difficult to measure experimentally, and there is currently no consensus on the exact value. One of the difficulties for accurate measurement in semiconductor or metallic materials is that the complex microstructure couples with the anisotropy of elastic modulus, so the elastic limit for specimens of different microstructures of the same material can be different [1].

Studies show that the breaking stress of silicon is measured to be around 1 GPa, with some variation depending on different sample preparation procedures [2]. Experimental measurements have shown that the fracture stresses of silicon wafers with thicknesses of several hundred microns are around several GPa [3], with maximum experimentally determined values of 175 MPa [4]. Other studies have shown experimentally that breaking/fracture of single-crystalline silicon occurs for fracture stresses between 40 and 110 MPa for various indent loads and flaw sizes [5]. Microstructuring of brittle materials such as Si leads to higher values of fracture stress than bulk because the crack/flaw size in microstructures is much smaller, according to Griffith's criterion [6]. Dislocation banding with up to 20% plastic deformation in float-zone silicon microstructures has been observed at room temperature from applied stresses of 5 GPa [7]. Studies show that superimposing a confining pressure of around 1.5 GPa on single-crystal silicon produces large plastic strains at 300 °C with up to about 1 GPa of yield stress [8].

2. Coherent x-ray diffraction (CXD) as a way to image strain

Here, we study the appearance of dislocations in bulk silicon by Bragg coherent x-ray diffraction imaging (BCDI), which is a sensitive method to probe these defect structures. A previous x-ray study [9] located the diffraction signal from a known dislocation loop by using coherent

micro-diffraction technique. The characteristic flares from the defect were tracked around the loop, but no inversion of the data was attempted to obtain images. More recently, the strain fields surrounding dislocation loops have been imaged by the scanning x-ray ptychography CXD technique [10].

In this work, we have imaged dislocations in silicon nanowires, fabricated using silicon-on-insulator (SOI) technology, during bending by radiation-induced swelling of an adjacent oxide layer. We introduce a method for phasing the diffraction patterns, guided-phase-error-reduction (GPER), which makes use of quantitative finite element analysis (FEA) calculations to constrain the phasing. We have observed mixed types of dislocations in the reconstructed nanowire following the highest dose of x-rays. An abrupt change immediately beyond this dose indicates that the nanowires undergo mechanical breakdown upon further x-ray exposure.

An advantage of BCDI [11, 12] over other microscopy methods for investigating strain is due to its enormous potential for probing large three-dimensional (3D) buried structures without the need for slicing 3D objects [13]. BCDI allows us to investigate strain on the nanoscale within objects in their as-prepared state. No destructive thinning or other sample preparation is required, as is necessary for transmission electron microscopy. BCDI is able to investigate strains, seen as displacements from the atomic positions of an ideal crystal lattice. It allows measurement of strains of individual structures (with dimensions from 10 nm to $> 1\,\mu$m) while other traditional x-ray diffraction techniques, such as reciprocal lattice mapping, obtain results by averaging many copies of the structure of interest [14].

3. Strong phase limit

The lattice strains present in deformed crystals result in a 'geometrical phase' in the images obtained by the CXD methods [13, 28]. The unstrained background lattice of the crystal defines the reference position with a zero phase in the complex electron density function obtained from the measurements. The diffracted wave from any portion of the crystal which is displaced from the reference position becomes advanced or retarded in phase by the projection of the displacement onto the diffraction vector, **Q**, usually approximated by a reciprocal lattice vector [13]. A phase shift of 2π corresponds to a displacement of one lattice spacing and is invisible, while the intermediate phase shifts resulting from the local relaxations surrounding classical lattice defects are visible.

Most coherent diffraction imaging (CDI) phasing procedures make use of iterative algorithms such as hybrid-input–output [15] and error reduction (ER) [16] to solve the diffraction phase problem, using the property that the diffraction pattern is oversampled with respect to the spatial Nyquist frequency. Once phased, the diffraction patterns are Fourier transformed to 3D real-space images. However, these iterative algorithms are often found to fail when phasing the diffraction patterns of highly strained objects, with the algorithms failing to converge. The algorithms typically start failing when the image phase goes beyond about $\pi/2$, corresponding to one quarter lattice constant displacements, and have considerable difficulty with π phase shifts where the amplitude of one region of the crystal tends to cancel the neighboring ones. Strong phase objects are those containing phases close to or greater than 2π such that the images appear 'wrapped'. The reason strong phase structures are difficult to phase is that the phase structure can become multivalued, hence potentially ambiguous in the solution. When this happens, the phase function has to be constrained to remain a smooth function of position, as our new GPER method attempts to achieve.

Phase 'vortices', in which the phase undergoes a 2π rotation around a closed line in three dimensions, are a common artifact of failed convergence of the algorithms; unfortunately these structures closely resemble the structure of the strain field expected surrounding a dislocation loop. It is common to constrain the phase of the image to avoid these failures [12].

Retrieving images from the CDI data measured from objects containing large strains is still under development, although there have been several successful attempts [14, 17]. Our GPER method uses calculated complex real-space models to guide iterative algorithms, leading to much better convergence. One reason strong-phase CDI is so difficult is the 'propagation non-uniqueness', whereby equivalent solutions can be generated by propagating along the optical axis, all of which possess the same far-field diffraction patterns [17, 18]. Since strain patterns in the sample and x-ray focusing artifacts can have similar phase distributions to an out of focus image, highly strained samples present a uniqueness problem to the phase retrieval algorithms which normally work in the case of lightly strained samples.

4. Experiment and results

### 4.1. Sample preparation of silicon on insulator nanowires

The SOI patterned structures used in our studies consisted of 170 nm thick Si thin films wafer bonded to a 1 μm thick SiO_2 layer grown on a bulk silicon substrate. Poly-methyl methacrylate resist was used for electron-beam lithography for patterning of our SOI structures with a lateral dimension of 800 nm and a length of 15 μm. Reactive ion etching (RIE) with SF_6 at a flow rate of 30 sccm and a dc voltage of 100 V was used to etch away the unwanted top layer. Arrays of Si nanowire structures were fabricated with overall dimensions of 15 μm $\times$ 800 nm $\times$ 170 nm (length$\times$width$\times$height). A slight undercutting of the resist, resulting in a tapered wire cross-section, was obvious in the obtained structures due to the RIE process.

4.2. Experiment

CDI measurements were performed at beamline 34-ID-C of the Advanced Photon Source at Argonne National Laboratory, with an x-ray energy of 8.9 keV selected with a Si (111) monochromator. The x-ray beam was cut to dimensions 30 and 50 μm by using slits to preserve the transverse coherence properties [19]. The coherent beam was then focused with horizontal and vertical Kirkpatrick–Baez (KB) mirrors. The size of the focus was measured to be slightly less than 1.5 μm in both directions using crossed tungsten wires scanned across the beam. A schematic drawing of the experimental geometry is shown in figure 1.

A confocal microscope [20] was used to pinpoint the specific nanowire structures to be measured. Off-specular (111) reflections of Si nanowires were chosen for CDI measurements and the incidence angle on the substrate was fixed to be $1°$. The long edge of the Si nanowire is along the (110) and the Q-vector is (111), inclined upward from the wire direction. The x-ray beam illuminates the wire approximately $25°$ from perpendicular and at grazing incidence to the substrate. The far-field diffraction intensity was measured by a charged coupled device detector with 20 μm pixels, placed 0.7 m away from the sample, orientated at the corresponding (111) Bragg angle. Rocking curves were taken with a range of $\pm 0.5°$ in the rocking angle with $0.02°$ increments, so that the oversampling conditions were fulfilled in all of the three dimensions.

We previously showed [21] that the underlying SiO_2 layer swells gradually after prolonged exposure to such a strongly focused x-ray beam and this causes a local bending of the nanowire
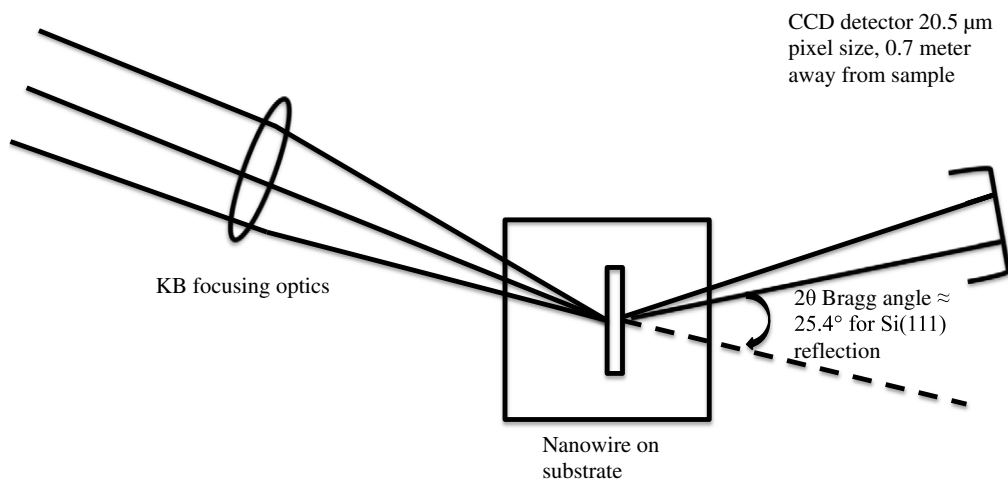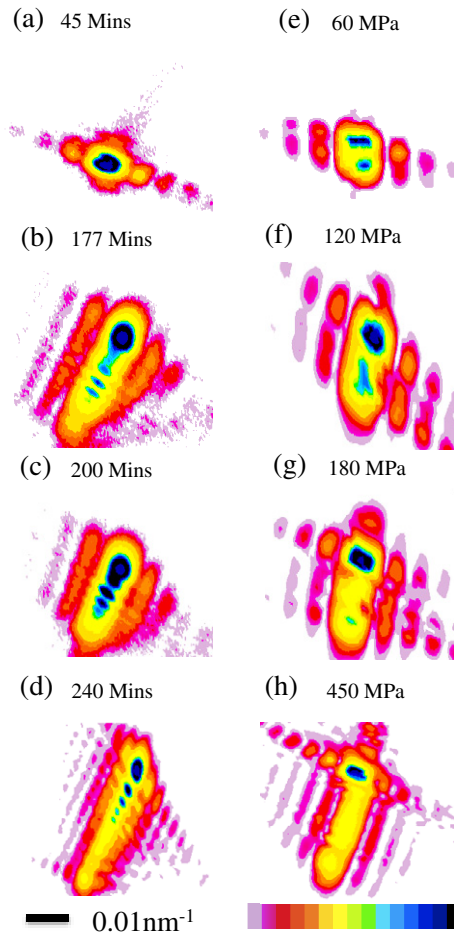
Figure 1. Schematic drawing of experimental geometry. Detector angle is at $\delta = 17.54°$ in-plane and $\gamma = 11°$ out of plane.

over the width of the beam (about $1\,\mu m$) in the middle of its length. A series of 20 measurements were made at intervals of 15 min to observe the evolution of the diffraction pattern. The total time required to record a 3D rocking curve scan was about 20 min. Our previous results show that the peak distribution width increased approximately linearly with exposure time. Cross-sectional slices through these 3D diffraction patterns are shown in figure 2 at representative times during the evolution. Figure 2(d) was the last recorded diffraction pattern before it disappeared. After 240 min of exposure, the measurement time was increased by a factor of 4 to achieve the same total integrated intensity as earlier measurements of the same nanowire. These measurements record the evolution of silicon nanowire as it is bent by the swelling of the underlying oxide under irradiation.

The irradiation behavior was reproducible and observed repeatedly on fresh wires [20]. It could be prevented by maintaining the sample in an inert He atmosphere, hence it was attributed to beam-induced oxidation of the substrate [20].

4.3. Finite-element-analysis (FEA) simulation

We also showed previously [21] that the redistribution of intensity in the Bragg peak, and notably the progressive splitting of its center into two distinct sidelobes during the time series, could be explained by bending of the SOI wire under radiation-induced stress from SiO_2. This was achieved by FEA using the COMSOL program. In this work we use that FEA model as a constraint in the GPER data fitting procedure. It was necessary to conduct FEA calculations in the same coordinate system as the measurements, so the simulated nanowires were rotated to the crystallographic orientation that was used in the experiment. A Gaussian x-ray probe with full width at half maximum of $1.5\,\mu m$, was then used to simulate the diffraction pattern. The Gaussian function was used to model the beam illuminating the sample in one direction only. In the other two (transverse) directions, the sample edges are well defined and fully illuminated. Along the length of the wire, the Gaussian is a fairly rough approximation to the central maximum only and ignores the sidelobes expected for the illumination profile. This is justified mainly because there is very little structure in the data along this direction, which is therefore

(a) 45 Mins   (e) 60 MPa

(b) 177 Mins   (f) 120 MPa

(c) 200 Mins   (g) 180 MPa

(d) 240 Mins   (h) 450 MPa

0.01nm^{-1}

Figure 2. Panels (a)–(d) are experimental diffraction patterns of a Si nanowire as a function of exposure time and (e)–(h) are corresponding simulated patterns as a function of peak applied stress.

less important than the other two directions. We have performed reconstructions with slightly different illumination profiles by variation of the Gaussian function full width at half maximum. Very little effect was observed in the final reconstruction results. If the exact structures of the sidelobes were known, then more accurate reconstruction results could in principle be obtained. Both simulated and measured data for various x-ray exposure doses are presented on the same sampling grid in figure 2.

4.4. Guided-phase error reduction iterative algorithm

Traditional phasing algorithms utilize a direct-space constraint in the form of a 'support', a volume of space in which the solution is allowed to exist. The GPER algorithm generalizes this idea to a 3D complex 'support', using the model as an additional direct-space constraint on phases. Since the traditional phasing algorithms converge well for images within $\pi/2$ of the correct answer, it was expected that an FEA model that comes within $\pi/2$ of the correct image phase at each location would be sufficient to guide the phase to the correct value. In this

work, we define the support amplitude by first estimating the auto-correlation function of the diffraction intensity, then gradually refine the support by testing and trying reconstructions.

In GPER, if the phase values at each voxel of the current iteration lie outside an allowed range defined by the FEA model they are set to those extreme values, otherwise the phase values are kept unchanged. Typical bounds were $\pm0.5\pi$ to $\pm0.9\pi$ depending on the datasets. This extra step is followed by the standard support constraint projection of the ER algorithm, whereby all of the density points outside the object boundary are set to zero. The phase constraint could be incorporated into a complex 'support' function, derived from the best-fitting FEA model that was used as the real-space constraint in the GPER algorithm.

Previous analyses by Huang [17] and Minkevich [14] have demonstrated the power of various direct-space constraints which have led to an improvement in convergence and better filling of the density of reconstructions from the CDI data of highly strained objects. Huang *et al* [17] discovered that implementation of phase-constraint in direct space is equivalent to the usage of a tight-support constraint and that application of both led to correctly focused solutions. Newton utilized a direct-space density gradient minimization method that is related to compressed sensing techniques [22]. In order to reconstruct highly strained CDI data, it is necessary to use *a priori* information about the sample [14]. Our method shares similarities with Fresnel CDI which utilizes a known curved illumination [23, 24] to avoid the twin confusion problem that is common in phase retrieval. Our method also bears strong similarity to phase retrieval in surface x-ray diffraction where a model of the bulk crystal is used as a reference in phase retrieval to produce an image of the surface structure [25].

5. Observation and interpretation of new structures

The best-fitting FEA model phase structures of SOI nanowire with various irradiation doses are illustrated in the top panel of figure 3. The phases were calculated by taking the scalar product of the displacement with the reciprocal-space Q-vector for the (111) crystallographic planes of the silicon nanowire. The phases shown in the top panel in figure 3 represent projected displacements resulting from strains induced from bending of the SOI nanowire, with applied stresses on the SiO_2 underneath the Si nanowire having the maximum values indicated. The diffraction patterns in figure 2 are the Fourier transforms of these model structures after adjusting the maximum applied stress value to agree with the data.

Figure 3 middle and bottom panels show amplitudes and phases (two-dimensional cross-sectional view cut-plane) of the final GPER reconstructions of the SOI nanowire with increasing x-ray radiation doses, from 45 to 240 min exposure time, respectively. The density is filled in reliably over the body of the nanowire, with some residual modulations associated with its strong phase structure. The two ends of the nanowire reconstructions are rough because the confined x-ray illumination between the ends of the nanowire, as observed previously [26]. The surface roughness of the reconstructed amplitude of the SOI nanowire might reveal the effects of the ions used to etch the sample surface, although other factors may contribute also.

We find that solutions are relatively stable after 30 iterations of GPER, the error-metric χ-square is relatively low, and calculated diffraction patterns have around 3% deviation from the measured data. Reconstructions performed starting with up to 25% values of applied Gaussian stresses of the FEA models all produce the main features, both phases and amplitudes, though some small derivations of the phase features are present. The supports used for the reconstruction were determined from the 3D autocorrelation of the data.
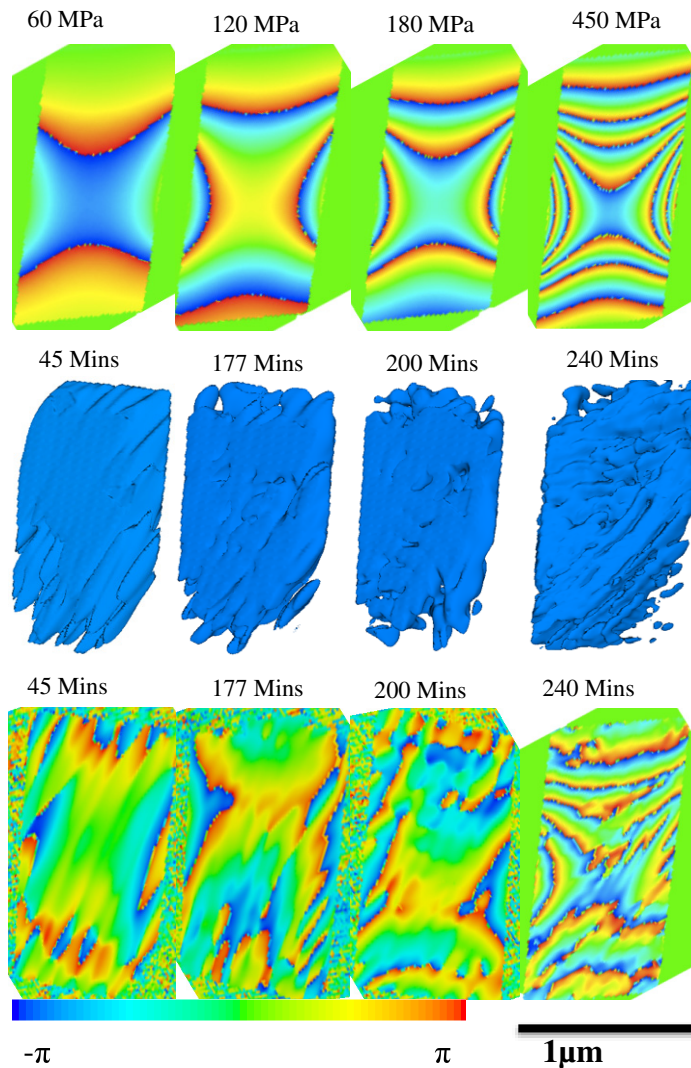
Figure 3. Top panel: cross-sectional view of the direct-space phase structures simulated in a nanowire by COMSOL FEA. Middle panel: iso-surface (with contourlevel of around 15% of maximum) of reconstructed amplitudes. Bottom panel: cross section of the reconstructed phases near the middle of the nanowire.

Our GPER method gives stable, reproducible results for some range of starting phase structures. To illustrate the performance, we performed convergence tests in figures 4 and 5. In figure 4, we varied the initial phase structure by varying the maximum Gaussian stress in the starting model from 350 to 550 MPa. All of the reconstructed phases have similar main features, with very little variations of small features. In figure 4, the resulting defect features are also shown to be reproducible when changing the initial phase structures used to seed the phasing algorithm, and with different initial random amplitude starts. Both of these results show that our reconstructions converge with a relatively high degree of reliability. To facilitate comparison of the reconstructed phases images, the phases were aligned by adding a constant offset. The main defect structures are found to be reproducible. There are some non-reproducible phase 'vortex'
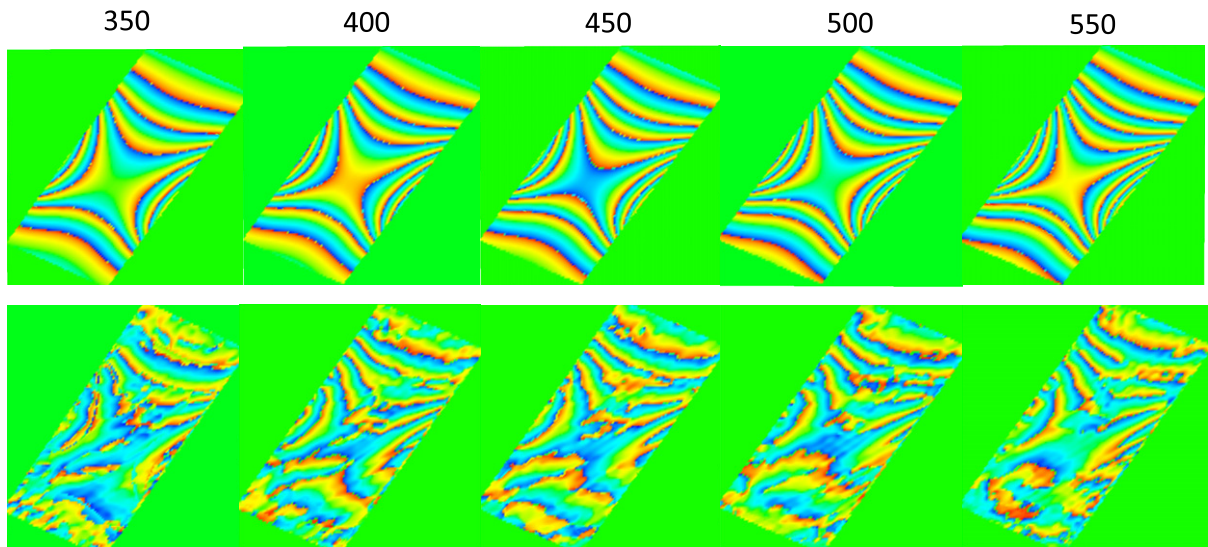
Figure 4. Reconstructions of the 240 min dataset starting from models with various applied maximum Gaussian stress values indicated (units are MPa). Top row: FEA simulated phase used to guide the phase in GPER. Bottom row: reconstructed phase. Phase offsets have been applied by adding a constant phase to compensate for the differences in the initial starting phases in the central region of the models.
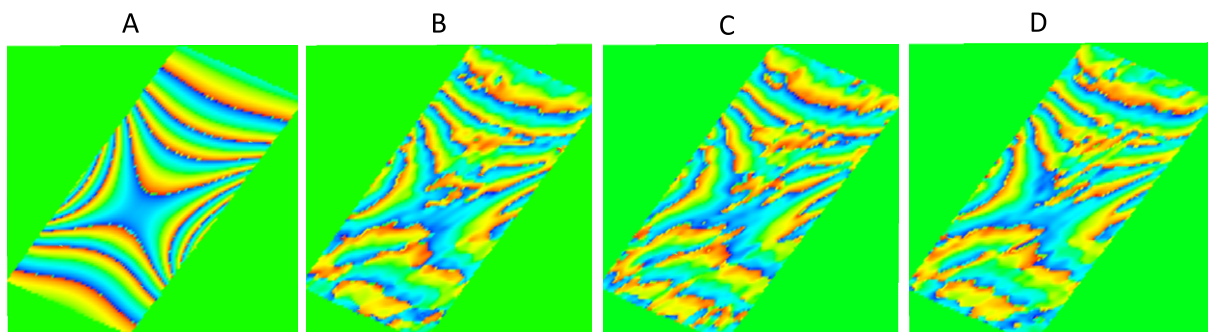
Figure 5. Convergence tests for different starting conditions of the algorithm on the 240 min data. (A) Model used to constrain the phase in GPER. (B) Final reconstruction starting with uniform amplitude inside the support and zero outside the support. (C), (D) Results of two different random starting amplitudes inside the support and zero outside the support.

structures at the very top and bottom of the images where the amplitude is very weak and the phase is noisy. These have been identified previously as a sign of poor convergence [27, 28]

We have performed simulation studies on the robustness of the GPER algorithm. Figure 6 shows that the radius of convergence of GPER is relatively limited: one needs to get very close phase models to correctly guide the reconstructions. Figure 6(B) shows the correct convergence when the phase in the center starts less than approximately 1.2 rad away from the correct value. However, in figure 6(C), when there are two extra phase wraps of discrepancy in the starting

A B C

Correct Phase model
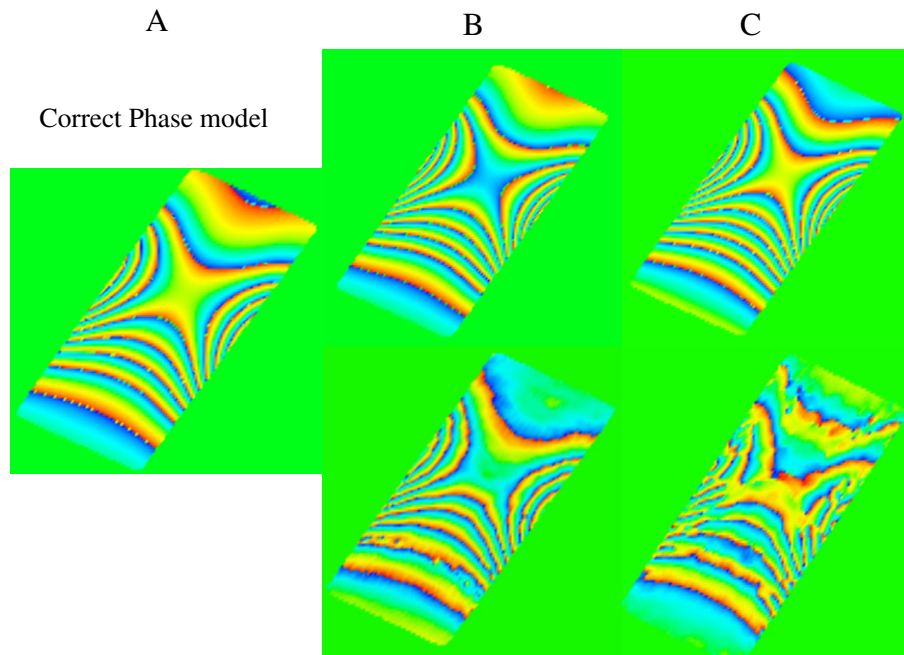
Figure 6. Simulation test of the GPER algorithm. Panel (A) shows the phase model used to simulate the data. Panel (B) shows a good reconstruction by using a close phase model as the guiding phase within the complex support (top: initial phase model; bottom: reconstructed phase). Panel (C) shows partially converged reconstruction by using a far-away phase model as the guiding support (top: initial phase model; bottom: reconstructed phase). There are approximately three more phase wraps in the starting model than the correct one.

phase model, only partially converged reconstruction results. Also, there is a strong coupling with the support: we previously showed that switching between planes of a two-plane object could be controlled by the choice of support [17].

To view the distortions associated with the last state of bending before fracture, we show an image of the difference between the phase of the FEA model and the reconstructed data for the 240 min x-ray dose in figure 7. Three characteristic phase structures have appeared, each with a distinct phase wrap ($-\pi$ to π) following an undulating plane traversing a localized region of the nanowire. Figures 7(b)–(d) show that these features are present throughout the thickness direction of the SOI nanowire, measured to be 160 nm, and extend over 200 nm laterally. It is a clear indication of the insertion or deletion of a single plane. This phase is a projection of the lattice distortions onto the (111) Q-vector, which points along the (110) long axis of the wire, and is inclined slightly above the plane. Such a phase wrap is a clear indication of the insertion of a single plane of atoms and the relaxation of the strain field surrounding it.

The origin of the phase wrap is illustrated in a model calculation in figure 8. An edge dislocation has a simple strain structure whose phase, the displacement projection onto a perpendicular Q-vector, is just equal to the angle around the dislocation edge [29]. Two parallel, opposite-signed dislocations represent a finite region of space containing an inserted (or deleted) plane of atoms. The superposition of the two strain fields is calculated in figure 8. At long range the stain cancels out, while close to the added plane it introduces a $+\pi$ phase shift on one side
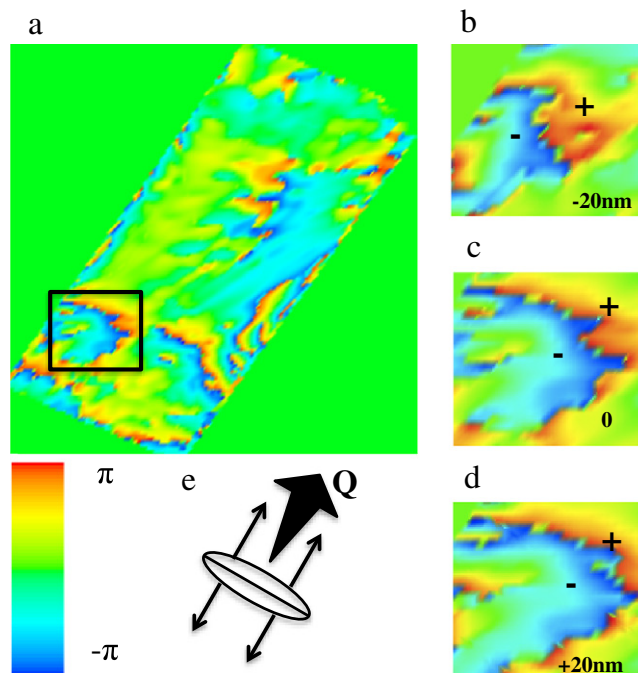
Figure 7. (a) Image of the difference between the phase of the FEA model and the reconstructed data for the 240 mins x-ray dose; (b)–(d) at the center and slices 20 nm above and below, (e) shows phase projection of the lattice distortions onto the (111) Q-vector, which points along the (110) long-axis of the wire, and inclined slightly above the plane as indicated by the black tapered arrow.

and $-\pi$ on the other side. A dislocation loop has a similar structure, but is confined in the third dimension as well. Hence, we identify these features as dislocation loops, viewed edge on, as indicated schematically in figure 7(e).

The two structures on the lower side of the wire are roughly planar, while the one on the upper side in figure 7 appears doubled, possibly by the merging of two nearby loops. It is important to note that only the component of lattice distortion along the (111) direction is resolved, hence, some parts of the structure may be concealed. There is also some noise in the images from the phase subtraction procedure, but the presence of phase wraps is very clear. Some of the jagged appearances could be due to relative movement of the beam and sample [30] or from fluctuations during the exposure. It is probably significant that all of the three dislocation loops have formed away from the central region of the highest beam intensity, very roughly at its half-maximum point, and that the phase wraps have opposite signs on the two sides. According to the model above of radiation induced swelling of the underlying oxide, these will be the points of maximum stress gradient with a significant shear component.

A previous coherent x-ray diffraction study of dislocations in bulk silicon showed a localized streaking of the Bragg peak whenever the scanned x-ray beam crossed over a dislocation loop [9]. The interpretation of the streaking was due to an extended planar structure trapped between two partial dislocations forming the loop, extending over several hundreds of nanometers. The authors of [9] have not presented any images of the structures obtained by inverting their diffraction patterns; direct comparison with our diffraction patterns is not possible because of the dominant contribution of bending in our data.
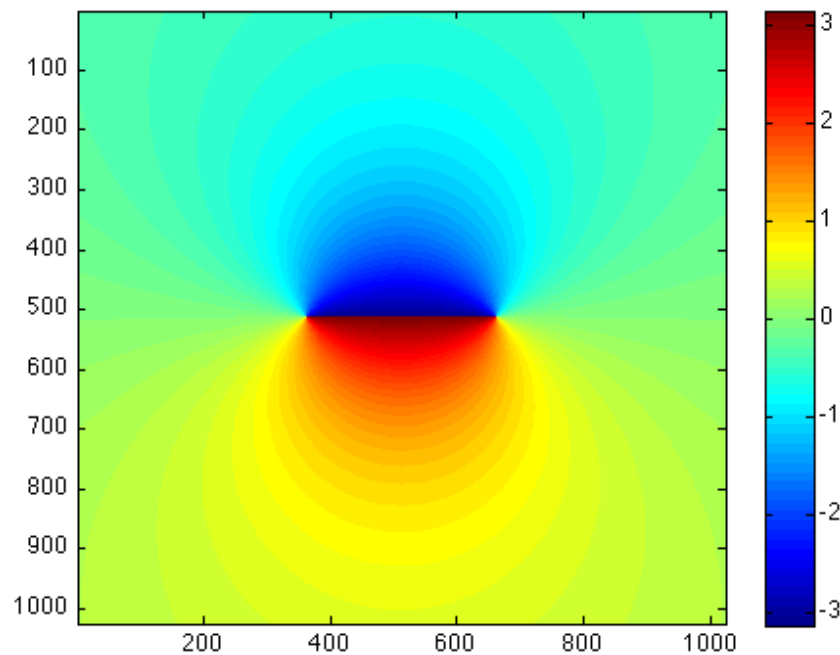
Figure 8. Simulation of the phase representing the projection of the displacement fields generated by two opposite dislocations a certain distance apart. The colorbar represents phases, which are the projection of local displacements onto a Q-vector running down the page. A phase wrap is generated in the vicinity of the added plane between the two dislocations.

The close agreement of the FEA model with the experimental data means that we can trust the input parameters quite well. The peak stress within the radiation-sensitive SiO_2 layer was 450 MPa for the case when the dislocation structures started appearing. This marks the beginning of plastic deformation and gives an estimate of the elastic limit of Si in this geometry. The COMSOL analysis allows us full access to the elastic stress-tensor components three dimensionally in the whole nanowire structure. Directly reading from our FEA model, the stress within the Si wire is highly anisotropic. The maximum stresses of the diagonal tensor components near the edges of the silicon nanowires were 330 MPa; the maximum shear stresses were around 176 MPa. This number for the elastic limit of Si is comparable with the experimental values for fracture stresses [4, 5]. It is possible that there may be some radiation-induced weakening of the Si, and also that there are unresolved artifacts of the RIE procedure used to make the nanowires giving rise to weak points in the structure.

6. Conclusion and future outlook

Imaging of 3D dislocations by high-resolution transmission electron microscopy [31] represents an important step toward the understanding of imperfection of semiconductor nanostructures. Previous studies on stacking faults/dislocations on metals suggest [32] that the deformation mechanism of metals is dependent on the ratio of stacking fault energy to unstable stacking fault energy. The studies also suggest that quantitative mapping of 3D deformation mechanism of metals or other materials in general purely by simulations is still at its infancy, because the

current simulation methods could only allow investigations on scenarios of high stress with short timescale [32]. Further experimental evidences have to be obtained along with theory to enable the complete understanding of plastic deformation of metals and other materials.

BCDI using Bragg peaks from crystalline samples is extremely strain sensitive and can be used to study highly strained objects. Various dislocation structures in silicon occur when the applied external stress is close to the elastic limit, i.e. when silicon begins to break. Dislocations, which can be edge, screw or a mixture of the two types, are found to be present in plastically deformed silicon of various types [33, 34]. Our observation of dislocations within SOI under high x-ray doses further demonstrates that BCDI is a good technique for analyzing dislocation/defects within nanostructures in a quantitative way. Strains and deformations of epitaxial SiGe have been observed in SOI micro-pad structures due to industrial processing [35] using x-ray ptychography [36]. This method should, in principle, be able to solve the strong phase CDI problem. The ptychography technique, especially in Bragg geometry, is still under development.

The cross-sectional shapes of the SOI nanowire structures are well-determined transverse to the wire direction. Here, the sample is smaller than the beam and can be assumed to be uniformly illuminated, entirely within its central maximum which has no phase. Along the wire direction, however, the shape is not well determined and shows ragged ends. This is understood to arise from the simplified modeling of the illumination profiles by a Gaussian function instead of the opposite-phase sidelobes expected for the KB mirror focusing system with a rectangular entrance aperture. In the future, it might be possible to gain further information by using the scanning Bragg ptychography method mentioned above [36].

Our studies have demonstrated the novelty of BCDI for successful probing of the evolution of nano-scale strains in nanostructured silicon with increasing x-ray radiation doses. The transformation of SOI nanowire structures can have a crucial influence on nanomechanics under various device-operating conditions, such as radiation, heat and pressure. Our work provides an improved understanding of the dislocation-forming processes in semiconductors in general, and this technique could be promising for pinpointing the underlying mechanisms that are responsible for observed improvements on carrier mobility in SOI-based electronic devices [37].

Acknowledgments

References

[1] Prohászka J, Mamalis A G and Gaál Z 2009 CIRP the cause of the uncertainty of the elastic limit *J. Manuf. Sci. Technol.* **2** 70
[2] Namatsu H, Kurihara K, Nagase M, Iwadate K and Murase K 1995 Dimensional limitations of silicon nanolines resulting from pattern distortion due to surface tension of rinse water *Appl. Phys. Lett.* **66** 2655
[3] Mclaughlin J C and Willoughby A F W 1987 Fracture of silicon wafers *J. Cryst. Growth* **85** 83

[4] Olson C R, Kuryliw E, Jones B E and Jones K S 2006 Effect of stress on the evolution of mask-edge defects in ion-implanted silicon *J. Vac. Sci. Technol.* B **24** 446

[5] Tsai Y L and Mecholsky J J Jr 1991 Fractal fracture of single crystal silicon *J. Mater. Res.* **6** 1248

[6] Griffith A A 1921 The phenomena of rupture and flow in solids *Phil. Trans. R. Soc.* A **221** 163

[7] Rabier J and Demenet J L 2001 On a change in deformation mechanism in silicon at very high stress: new evidences *Scr. Mater.* **45** 1259

[8] Castaing J, Veyssière P, Kubin L P and Rabier J 1981 The plastic deformation of silicon between 300 and 600 °C *Phil. Mag.* A **44** 1407

[9] Jacques V, Ravy S, Le Bolloc'h D, Pinsolle E, Sauvage-Simkin M and Livet F 2011 Bulk dislocation core dissociation probed by coherent x-rays in silicon *Phys. Rev. Lett.* **106** 065502

[10] Takahashi Y, Suzuki A, Furutaku S, Yamauchi K, Kohmura Y and Ishikawa T 2013 Bragg x-ray ptychography of a silicon crystal: visualization of the dislocation strain field and the production of a vortex beam *Phys. Rev.* B **87** 121201

[11] Williams G, Pfeifer M, Vartanyants I and Robinson I 2003 Three-dimensional imaging of microstructure in Au nanocrystals *Phys. Rev. Lett.* **90** 17

[12] Pfeifer M A, Williams G J, Vartanyants I A, Harder R and Robinson I K 2006 Three-dimensional mapping of a deformation field inside a nanocrystal *Nature* **442** 63

[13] Robinson I and Harder R 2009 Coherent x-ray diffraction imaging of strain at the nanoscale *Nature Mater.* **8** 291

[14] Minkevich A A, Fohtung E, Slobodskyy T, Riotte M, Grigoriev D, Metzger T, Irvine A C, Novák V, Holý V and Baumbach T 2011 Strain field in (Ga,Mn)As/GaAs periodic wires revealed by coherent x-ray diffraction *Europhys. Lett.* **94** 66001

[15] Fienup J R 1982 Phase retrieval algorithms—a comparison *Appl. Opt.* **21** 2758

[16] Gerchberg R W and Saxton W O 1972 A practical algorithm for the determination of phase from image and diffraction plane pictures *Optik* **35** 2

[17] Huang X, Harder R, Xiong G, Shi X and Robinson I 2011 Propagation uniqueness in three-dimensional coherent diffractive imaging *Phys. Rev.* B **83** 224109

[18] Spence J C H, Howells M, Marks L D and Miao J 2001 Lensless imaging—a workshop on 'new approaches to the phase problem for non-periodic objects' *Ultramicroscopy* **90** 1

[19] Libbert J L, Pitney J A and Robinson I K 1997 Asymmetric Fraunhofer diffraction from roller-blade slits *J. Synchrotron Radiat.* **4** 125

[20] Beitra L, Watari M, Matsuura T, Shimamoto N, Harder R and Robinson I 2010 Confocal microscope alignment of nanocrystals for coherent diffraction imaging *AIP Conf. Proc.* **1234** 57

[21] Shi X, Xiong G, Huang X, Harder R and Robinson I 2012 Radiation-induced bending of silicon-on-insulator nanowires probed by coherent x-ray diffractive imaging *New J. Phys.* **14** 063029

[22] Newton M, Harder R, Huang X, Xiong G and Robinson I 2010 Phase retrieval of diffraction from highly strained crystals *Phys. Rev.* B **82** 165436

[23] Williams G, Quiney H, Dhal B, Tran C, Nugent K, Peele A, Paterson D and de Jonge M 2006 Fresnel coherent diffractive imaging *Phys. Rev. Lett.* **97** 025506

[24] Abbey B, Nugent K A, Williams G J, Clark J N, Peele A G, Pfeifer M A, de Jonge M and McNulty I 2008 Keyhole coherent diffractive imaging *Nature Phys.* **4** 394

[25] Saldin D K, Harder R J, Shneerson V L and Moritz W 2001 Phase retrieval methods for surface x-ray diffraction *J. Phys.: Condens. Matter* **13** 10689

[26] Xiong G, Huang X, Leake S, Newton M C, Harder R and Robinson I K 2010 Coherent x-ray diffraction imaging of ZnO nanostructures under confined illumination *New J. Phys.* **13** 033006

[27] Fienup J R and Wackerman C C 1986 Phase-retrieval stagnation problems and solutions *Opt. Soc. Am.* **3** 1897

[28] Marchesini S 2007 Phase retrieval and saddle-point optimization *J. Opt. Soc. Am.* A **24** 10

[29] Hytch M, Houdellier F, Hue F and Snoeck E 2008 Nanoscale holographic interferometry for strain measurements in electronic devices *Nature* **453** 1086

IOP Institute of Physics   **Φ** DEUTSCHE PHYSIKALISCHE GESELLSCHAFT

[30] Clark J N, Putkunz C T, Curwood E K, Vine D J, Scholten R, McNulty I, Nugent K A and Peele A G 2011 Dynamic sample imaging in coherent diffractive imaging *Opt. Lett.* **36** 1954

[31] Barnard J S, Sharp J, Tong J R and Midgley P A 2006 High-resolution three-dimensional imaging of dislocations *Science* **313** 319

[32] Van Swygenhoven H, Derlet P M and Froseth A G 2004 Stacking fault energies and slip in nanocrystalline metals *Nature Mater.* **3** 399

[33] Dash W C 1958 Evidence of dislocation jogs in deformed silicon *J. Appl. Phys.* **29** 705

[34] Eymery J, Buttard D, Fournel F, Moriceau H, Baumbach G and Lübbert D 2002 Dislocation strain field in ultrathin bonded silicon wafers studied by grazing incidence x-ray diffraction *Phys. Rev.* B **65** 165337

[35] Hruszkewycz S O, Holt M V, Murray C E, Bruley J, Holt J, Tripathi A, Shpyrko O G, McNulty I, Highland M J and Fuoss P H 2012 Quantitative nanoscale imaging of lattice distortions in epitaxial semiconductor heterostructures using nanofocused x-ray Bragg projection ptychography *Nano Lett.* **12** 5148–54

[36] Rodenburg J M, Hurst A C, Cullis A G, Dobson B R, Pfeiffer F, Bunk O, David C, Jefimovs K and Johnson I 2007 Hard-x-ray lensless imaging of extended objects *Phys. Rev. Lett.* **98** 034801

[37] Xiang J, Lu W, Hu Y, Wu Y, Yan H and Lieber C M 2006 Ge/Si nanowire heterostructures as high-performance field-effect transistors *Nature* **441** 489